

1 **Droplet collection efficiencies ~~estimated~~inferred from satellite**  
2 **retrievals constrain effective radiative forcing of aerosol-cloud**  
3 **interactions**

4 Charlotte M. Beall<sup>1</sup>, Po-Lun Ma<sup>1</sup>, Matthew W. Christensen<sup>1</sup>, Johannes Mülmenstädt<sup>1</sup>, Adam  
5 Varble<sup>1</sup>, Kentaroh Suzuki<sup>2</sup>, Takuro Michibata<sup>3</sup>

6 <sup>1</sup>Atmospheric Sciences and Global Change Division, Pacific Northwest National Laboratory, Richland, WA, 99354,  
7 U.S.A.

8 <sup>2</sup>Atmosphere and Ocean Research Institute, University of Tokyo, Chiba, 277-8568, Japan

9 <sup>3</sup>Department of Earth Science, Okayama University, Okayama, 700-8530, Japan

10 *Correspondence to:* Charlotte M. Beall; charlotte.beall@pnnl.gov

11  
12 **Abstract.** Process-oriented observational constraints for the anthropogenic effective radiative forcing due to aerosol-  
13 cloud-interactions (ERF<sub>aci</sub>) are highly desirable because the ~~large~~ uncertainty associated with ERF<sub>aci</sub> poses a  
14 significant challenge to climate prediction. The ~~satellite-based~~ Contoured Frequency by Optical Depth Diagrams  
15 (CFODD) analysis ~~was previously proposed to support~~s evaluation of model representation of cloud liquid to rain  
16 conversion processes because the slope of a CFODD, generated from joint MODerate Resolution Imaging  
17 Spectroradiometer (MODIS)-CloudSat cloud retrievals, provides an estimate of cloud droplet collection efficiency in  
18 single-layer warm liquid clouds (~~SLWCs~~). Here we present an updated CFODD analysis as an observational constraint  
19 for the ERF<sub>aci</sub> due to warm rain processes and apply it to the U.S. Department of Energy's Energy Exascale Earth  
20 System Model version 2 (E3SMv2). ~~Updates to the CFODD analysis include multiple changes to the SLWC detection~~  
21 ~~algorithm for better consistency between MODIS-CloudSat observations and the satellite simulators, as well as the~~  
22 ~~estimation of CFODD slopes using Random Sample Consensus robust linear regression.~~A series of sensitivity  
23 experiments shows that E3SMv2 droplet collection efficiencies and ERF<sub>aci</sub> are highly sensitive to ~~the treatment of~~  
24 autoconversion, the rate of mass transfer from cloud liquid to rain, yielding a strong correlation between the CFODD  
25 slope and the shortwave component of ERF<sub>aci</sub> (~~ERF<sub>aci,sw</sub>~~; Pearson's R = -0.91). We estimate ~~ERF<sub>aci,sw</sub>~~the shortwave  
26 ~~component of ERF<sub>aci</sub> (ERF<sub>aci,sw</sub>)~~, constrained by MODIS-CloudSat, by calculating the intercept of the linear  
27 association between ~~the ERF<sub>aci,sw</sub> E3SMv2 ERF<sub>aci,sw</sub>~~ and the CFODD slopes, using the MODIS-CloudSat CFODD  
28 slope as a reference. When E3SMv2's ~~droplet collection efficiency~~CFODD slope is constrained to agree with the A-  
29 Train retrievals, ERF<sub>aci,sw</sub> is reduced by ~~143 ± 6%~~ in magnitude, indicating that correcting bias in the ERF<sub>aci,sw</sub> due  
30 to autoconversion would bring E3SMv2's total ERF<sub>aci</sub> (-1.50 W m<sup>-2</sup>) into better agreement with the IPCC AR6 'very

Formatted: Subscript

Formatted: Subscript

31 likely' range for ERFaci ( $-1.0 \pm 0.7 \text{ W m}^{-2}$ ). ~~This study provides a new process-oriented observational constraint for~~  
32 ~~ERFaci due to warm rain processes to reduce the uncertainty of climate predictions.~~

## 34 1 Introduction

35 Single-layer, low-level marine warm clouds cover 25% of the ocean surface (Charlson et al., 1987) and exert a strong  
36 cooling effect on climate due to their reflectivity (Hartmann et al., 1992; Hartmann and Short, 1980; Ramanathan et  
37 al., 1989). Aerosols modulate multiple radiative properties of low warm clouds, including droplet number  
38 concentration ( $N_d$ ), liquid water path (LWP), geometric , cloud fraction, and lifetime, and their net impact on the cloud  
39 radiative forcing is the most uncertain component of the climate system (e.g., Stevens and Feingold, 2009;  
40 Christensen et al., 2020; Glassmeier et al., 2021). Though aerosols also exert a significant influence on ice and mixed-  
41 phase clouds, aerosol-cloud interactions (ACI) make their largest contribution to global radiative forcing via liquid  
42 water clouds (Bellouin et al., 2020).

43 In marine warm cloud regimes, an increase in aerosol concentrations typically leads to increasing  $N_d$ . Given constant  
44 condensed water content, enhanced aerosol concentrations increase cloud albedo due to higher concentrations of  
45 smaller cloud droplets through the so-called "Twomey effect" (Twomey, 1974). However, the cooling effect of  
46 increased  $N_d$  can be offset or enhanced by competing aerosol-mediated cloud properties such as cloud fraction and  
47 LWP. For example, increased numbers of smaller droplets can diminish cloud fraction by reducing cloud droplet  
48 sedimentation (Bretherton et al., 2007) and increasing cloud-top evaporation and dry air entrainment (Wang et al.,  
49 2003). On the other hand, aerosols can also increase cloud fraction and vertical extent by suppressing precipitation  
50 (Albrecht, 1989; Pincus and Baker, 1994). Christensen et al. (2020) demonstrated that the impact of aerosol on low-  
51 level cloud areal coverage depends on the stability of the atmosphere: in thermodynamically stable lower tropospheric  
52 conditions, increased aerosol results in increased cloud fraction, lifetime and  $N_d$ , whereas in unstable conditions,  
53 entrainment and evaporation offset Twomey effects, resulting in relatively smaller changes to cloud radiative  
54 properties.

55 Earth Systems Models (ESMs) are relied upon for estimating the global Effective Radiative Forcing of Aerosol-Cloud  
56 Interactions (ERFaci) due to the dearth of observations from the pre-industrial era. Yet ESM estimates are challenged  
57 by the lack of observational constraints on ERFaci and the cloud processes that modulate ERFaci, which must be

58 parameterized due to the computational expense of explicitly resolving them. Mülmenstädt et al. (2020) proposed a  
59 renewed focus on process-oriented observational constraints as a solution to “equifinality”, whereby differing  
60 representations of cloud processes can reproduce observed state variables such as LWP and cloud fraction. The  
61 problem of equifinality renders many global long-term observations of state variables useless for constraining ERFaci  
62 on their own. Mülmenstädt et al. (2020) argues that constraints based on cloud process observations are thus highly  
63 desirable as an alternative approach to state variable-based constraints because mitigating bias in a cloud process  
64 representation will improve estimates of the response of the process to aerosols. Process-oriented constraints on  
65 ERFaci are useful for quantifying the sensitivity of ERFaci to a specific process or constraining the component of  
66 ERFaci that is affected by a process, rather than for constraining ERFaci overall (Mülmenstädt and Feingold, 2018).  
67 Recent examples of process-based diagnostics include the Earth System Model Aerosol-Cloud Diagnostics Package  
68 (ESMAC Diags) (Tang et al., 2022; Tang et al., 2023), which supports evaluation of aerosol activation processes, and  
69 Varble et al. (2023) which demonstrated multiple model-observations comparison approaches that target processes  
70 affecting cloud albedo susceptibility using geostationary satellite data and surface-based observations. Christensen et  
71 al. (2023) applied ground-based measurements, satellite retrievals and meteorological reanalysis products in a  
72 Lagrangian framework to evaluate multiple aerosol-cloud processes in E3SM, including cloud condensation nuclei  
73 deposition via precipitation and the temporal response in  $N_d$  to aerosol perturbations.

74 In response to the demand for process-oriented constraints on warm liquid cloud processes, we present a constraint on  
75 the shortwave component of ERFaci (ERFaci<sub>sw</sub>) due to autoconversion, a parameterization representing the transfer  
76 of liquid mass and number from the cloud to rain category, based on satellite cloud retrievals. For the past 12 years,  
77 prior studies have applied the Contoured Frequency by Optical Depth Diagrams (CFODD) analysis (Nakajima et al.  
78 2010; Suzuki et al. 2010) to evaluate model representation of warm rain processes because the slopes of CFODDs,  
79 generated from spaceborne radar reflectivity profiles (CloudSat) (e.g. Marchand et al., 2008) and cloud property  
80 retrievals from the Moderate Resolution Imaging Spectroradiometer (MODIS) (e.g. Platnick et al., 2017), provide an  
81 estimate of cloud droplet collection efficiency in warm liquid clouds (Suzuki et al. 2010). Here we demonstrate ~~to~~  
82 demonstrate how an updated CFODD analysis can be applied to constrain ERFaci due to autoconversion using, we  
83 apply an updated CFODD analysis to MODIS-CloudSat retrievals between June 2006 and April 2011 as well as the  
84 U.S. Department of Energy’s Energy Exascale Earth System Model version 2 (E3SMv2) and the relationship between  
85 CFODD slopes and ERFaci<sub>sw</sub> in SLWCs, in a series of autoconversion sensitivity experiments. We show that the

Formatted: Subscript

Formatted: Subscript

Formatted: Not Superscript/ Subscript

86 shortwave component of  $ER_{Fac}$  ( $ER_{Fac_{sw}}$ ) can be constrained using the correlation between  $ER_{Fac_{sw}}$  and CFODD  
87 slopes (i.e., the slope computed from the in-cloud optical depth and CloudSat radar reflectivity, see Fig. 7 of Suzuki  
88 et al. 2010) using the MODIS-CloudSat CFODD slope as a reference.

89 To support the application of CFODD analysis as a constraint on  $ER_{Fac_{sw}}$ , we modified the Warm Rain Diagnostics  
90 (WRDs) subroutine (Michibata et al. 2019) that was recently implemented in the Cloud Feedback Model  
91 Intercomparison Project (CFMIP) Observations Simulator Package (COSPV2.0), a software package that supports  
92 climate model evaluation against satellite observations (Michibata et al., 2019; Swales et al., 2018). The WRDs  
93 support evaluation of model warm rain processes in single-layer warm liquid clouds (SLWCs) based on joint statistics  
94 from MODIS and CloudSat. The first diagnostic provides the fractional occurrence of SLWCs, classified as non-  
95 precipitating, drizzling, or raining clouds based on CloudSat column maximum radar reflectivity. The second  
96 diagnostic is the CFODD, which is the probability density function (PDF) of radar reflectivity as a function of in-  
97 cloud optical depth (ICOD), where ICOD is the optical depth integrated from the cloud top downward to each vertical  
98 layer and represents an in-cloud vertical coordinate (Nakajima et al., 2010; Suzuki et al., 2010). The CFODD shows  
99 how vertical cloud microphysical structures transition from non-precipitating to precipitating as a function of cloud-  
100 top effective radius ( $R_e$ ), and the slope of reflectivity change with ICOD provides an estimate of droplet collection  
101 efficiency factor (Suzuki et al., 2010). Previous studies have used CFODDs to demonstrate that pollution decreases  
102 droplet collection efficiency, suppressing rainfall near the cloud base (Mangla et al., 2020; Michibata et al., 2014;  
103 Suzuki et al., 2013), and to evaluate model cloud liquid to rain conversion processes against satellite observations  
104 (Suzuki et al., 2015; Jing et al. 2019; Michibata and Suzuki, 2020). Takahashi et al. (2021) proposed an updated  
105 CFODD analysis in which  $R_e$  thresholds are defined by quartile distributions of SLWC samples rather than the  
106 traditional CFODD  $R_e$  thresholds to focus evaluation on warm rain process representation rather than the bias in  $R_e$   
107 distribution. Modifications to the WRDs in the present study include additional diagnostics that provide SLWC  
108 sampling statistics to illuminate how sample size affects CFODD results, the implementation of a CloudSat ground-  
109 clutter mask in the simulated WRDs and updates to SLWC selection criteria for better consistency between  
110 observations and satellite simulators. The updated CFODD analysis is demonstrated here as a constraint on the  
111 component of  $ER_{Fac_{sw}}$  that is affected by droplet collection efficiency due to autoconversion.

## 112 2 Warm Rain Diagnostics Overview

Formatted: Subscript

Formatted: Subscript

Formatted: Subscript

Formatted: Subscript

113 The WRDs and their implementation in COSPv2.0 were described in Michibata et al. (2019). The WRDs are designed  
114 to run online with the host model, accumulating time step statistics on warm rain cloud processes for subcolumns to  
115 mitigate the risk of data-processing bottlenecks associated with outputting large data volumes. COSPv2.0 generates  
116 ensembles of stochastic subcolumns from model gridbox-mean variables to emulate model subgrid variability and to  
117 resolve discrepancies in spatial resolution between observations and the model grid (Swales et al., 2018).

118 To generate observational reference data for model evaluation, Michibata et al. (2019) used the MODIS and CloudSat  
119 products 2B-TAU R04 (Polonsky, 2008) and 2B-GEOPROF R04 (Mace et al., 2007; Marchand et al., 2008),  
120 respectively, for SLWC detection between June 2006 and April 2011. The ~~criteria for~~ SLWC detection are described  
121 in Supplement Table S1 and include CloudSat reflectivity  $\geq -30$  dBZ, MODIS liquid COT  $> 0.3$ , and cloud top  
122 temperature  $\geq 273$  K. Model-simulated SLWCs are detected using COSPv2.0 simulated CloudSat reflectivity and  
123 multiple MODIS cloud properties, including ice water path (IWP), liquid water path (LWP), cloud-top effective radius  
124 ( $R_e$ ), and cloud optical thickness (COT) (Table S1). For the SLWC fractional occurrence (frequency) diagnostic,  
125 SLWCs are binned by precipitation intensity according to the maximum column CloudSat reflectivity ( $Z_{max}$ ), where  
126 non-precipitating, drizzling and raining SLWCs correspond to  $Z_{max} < -15$  dBZ<sub>e</sub>,  $-15$  dBZ<sub>e</sub>  $\leq Z_{max} < 0$  dBZ<sub>e</sub>,  
127 and  $Z_{max} \geq 0$  dBZ<sub>e</sub>, respectively. The SLWC fractional occurrence diagnostic features frequency of each  
128 precipitation type relative to the total SLWC population.

129 To support evaluation of liquid cloud collection efficiencies and cloud to rain transition processes, CFODDs are  
130 constructed from the PDFs of CloudSat reflectivity profiles binned by ICOD. ICOD ( $\tau_d$ ) is parameterized as a function  
131 of MODIS COT ( $\tau_c$ ) by invoking the adiabatic condensation growth model to vertically slice the column  
132 COT into each layer (Suzuki et al., 2010). The relationship between  $\tau_d$  and  $\tau_c$  is as follows:

$$\tau_d(h) = \tau_c \left\{ 1 - \left( \frac{h}{H} \right)^{5/3} \right\} \quad (1)$$

135 where  $h$  is height and  $H$  is the geometric height of the cloud. The detailed derivation of the ICOD coordinate is  
136 provided in Suzuki et al. (2010). ~~by invoking the adiabatic condensation growth model to vertically slice the column~~  
137 COT into each layer (Suzuki et al., 2010). The slope of the resulting 2D-PDF diagnostic yields an estimate of is  
138 modulated by droplet collection efficiency, with steeper slope implying higher efficiency. The CFODD shows where,

Formatted: Font: 10 pt

Formatted: Font:

Formatted: Subscript

Formatted: Not Superscript/ Subscript

Formatted: Subscript

Formatted: Not Superscript/ Subscript

139 with ICOD on the y-axis as a vertical coordinate, the droplet collection efficiency increases, and where the transition  
140 from non-precipitating to drizzling and raining occurs, using the radar reflectivity as a proxy for the precipitation rate  
141 as described above (e.g., Muhlbaeuer et al., 2014). CFODDs are also typically binned by  $R_e$  to reveal how droplet  
142 collection efficiency changes with droplet size (Suzuki et al., 2010; Takahashi et al., 2021; Jing et al., 2017).

Formatted: Subscript

143 In this study, CFODD slopes are estimated using RANdom SAMple Consensus (RANSAC) robust linear regression  
144 (Fischler et al., 1987). RANSAC was chosen for performing linear regression due to the right-skewed distribution of  
145 CFODD datasets. The regression ~~is was applied to the CFODD distribution to the MODIS-CloudSat profiles and~~  
146 E3SMv2 output at  $4 \leq \text{ICOD} \leq 20$  and  $Z < 20$  dBZ. For E3SMv2 output, the regression was applied to approximated  
147 source CloudSat reflectivity and ICOD data that was estimated from time-mean CFODD frequencies. The reflectivity  
148 and ICOD thresholds were were chosen to reduce the effect of the Mie scattering regime where the radar reflectivity  
149 can be saturated and to restrict analysis to profiles where the uncertainty of MODIS COT retrievals is lower as error  
150 can be higher in optically thin liquid clouds (e.g.,  $\text{COT} < 4$ ) (Platnick et al., 2017). The uncertainty in the RANSAC  
151 slope calculation is estimated by “bootstrapping”, repeatedly performing RANSAC regressions on 1000 random  
152 subsamples of 80% the CFODD dataset to generate a distribution of slope estimates. The 1-sigma error and 95%  
153 confidence intervals were calculated from this distribution. The residual threshold applied for RANSAC outlier  
154 detection was 0.1 and 0.5 ~~xx~~ median absolute error (MAE) for MODIS-CloudSat and E3SMv2, respectively. Data  
155 points with MAE exceeding the residual threshold are excluded from the linear regression in RANSAC.

## 156 2.1 E3SMv2

157 Several updates to the WRDs are described in Sect. 2.2, the impacts of which are demonstrated through an application  
158 of the updated WRDs to the U.S. Department of Energy’s Energy Exascale Earth System Model v2 (E3SMv2). The  
159 atmosphere component of the model, E3SM Atmosphere Model v2 (EAMv2), is described in detail in Golaz et al.  
160 (2022). Like its predecessor EAMv1, EAMv2 predicts stratiform and shallow cumulus cloud macrophysics through  
161 the Cloud Layers Unified by Binormals (CLUBB) parameterization, which unifies the treatment of planetary boundary  
162 layer turbulence, shallow convection, and cloud macrophysics through a higher-order turbulence closure scheme  
163 (Bogenschutz et al., 2013; J. C. Golaz et al., 2002; Larson, 2017; Larson & Golaz, 2005). CLUBB diagnoses cloud  
164 fraction and cloud liquid water from a joint double-Gaussian PDF. Ice and liquid cloud fractions in CLUBB are  
165 analytically diagnosed by integrating saturated proportions of the joint PDF (Guo et al. 2015).

166 Cloud microphysics is represented with the “Morrison and Gettelman version 2” (MG2) scheme (Gettelman and  
167 Morrison, 2015). MG2 prognoses the mass mixing ratios and number concentrations of cloud liquid, ice and  
168 precipitation hydrometeors. The coupled MG2 cloud microphysics and CLUBB higher-order turbulence  
169 parametrization explicitly provides values for hydrometer mass and number mixing ratios as well as cloud fraction.  
170 Deep convection is represented by the Zhang and McFarlane (1995) (ZM) scheme. As convective cloud fraction is  
171 not parameterized in the mass-flux based ZM scheme, it is diagnosed from the cloud mass flux for cloud radiation  
172 calculation (Hack et al., 1993). The total cloud fraction in EAMv2 combines CLUBB, deep convective cloud fractions  
173 and ice cloud fraction following (Park et al., 2014). The four-mode version of the Modal Aerosol Module (MAM4) is  
174 used to predict aerosol properties and processes (Liu et al., 2012, 2016; H. Wang et al., 2020).

175 EAMv2 runs on 72 vertical atmospheric levels with a top at 0.1h Pa (Rasch et al., 2019; Xie et al., 2018). However,  
176 distinct from its predecessor EAMv1, EAMv2 has two separate parameterized physics and dynamics grids (Hannah  
177 et al., 2021), with average horizontal grid spacings of ~165 km and ~110 km, respectively.

178 A six-year E3SMv2 simulation with transient, present-day forcing was run between 2006 and 2011 with online  
179 COSPv2.0 for comparison with A-Train observations of SLWCs, allowing one additional year (2005) for model spin-  
180 up. To facilitate comparison with observations, large-scale winds were constrained via the “nudging” technique (Lin  
181 et al., 2016; Ma et al., 2014; Zhang et al., 2014), in which horizontal and vertical winds are relaxed toward the Modern  
182 Era-Retrospective Analysis for Research and Applications, Version 2 (MERRA2) reanalysis data (Gelaro et al., 2017)  
183 with a 6-hour time-scale. MERRA2 data are read in every 3 hours and linearly interpolated to model times. COSPv2.0  
184 is called at every time step (0.5 h) and run with 10 subcolumns. We observed little change in CFODD results for  
185 increased numbers of subcolumns of 20 to 50.

## 186 **2.2 COSPv2.0**

187 Cloud-observing instrument simulators support evaluation of model cloud representation by translating gridbox-mean  
188 model variables (e.g., cloud fraction, hydrometeor mass mixing ratio, precipitation) into quantities that are measured  
189 by a cloud sensor (e.g., reflectivity). COSPv2.0 includes multiple cloud-observing satellite simulators and has been  
190 used extensively to diagnose issues in model cloud representation (Cesana & Chepfer, 2012; Kay et al., 2016; Song  
191 et al., 2018a; Y. Zhang et al., 2010). Recently, M. Zhang et al. (2022) used the COSPv2.0 CALIPSO simulator to

192 demonstrate that changes to the Wegener-Bergeron-Findeisen process in EAMv2 decreased an ice cloud fraction low  
193 bias in the Arctic compared to EAMv1 but did not correct excesses of supercooled liquid.

194 There are known limitations to COSPv2.0 that affect its application to E3SM for cloud representation evaluation. The  
195 subgrid distribution of cloud variables generated by COSPv2.0 does not match E3SM subgrid variability.  
196 Hydrometeor species are distributed homogeneously across the subcolumns generated by COSPv2.0 via the  
197 subcolumn generator SCOPS (Subcolumn Cloud Overlap Profile Sampler) (Klein and Jakob, 1999), such that the  
198 ensemble of subcolumns reproduces the gridbox cloud fraction but not the subgrid distribution of liquid and ice within  
199 the simulated clouds (Dewald, 2021). Song et al., (2018b) demonstrated that the default “homogeneous hydrometeor  
200 scheme” from SCOPS results in overestimation of radar reflectivity in warm liquid clouds, thus overestimating  
201 precipitating clouds since maximum column reflectivity is often used to distinguish precipitating clouds (as in the  
202 WRDs). Errors in simulated satellite retrievals have also been attributed to SCOPS overlap assumptions (Hillman et  
203 al., 2018). Such a bias from SCOPS can result in unfair observational evaluation of a host model such as E3SMv2.  
204 Inconsistencies in microphysical assumptions between the host model and COSP pose another challenge. While many  
205 microphysical assumptions in COSPv2.0 can be configured for agreement with E3SMv2 microphysics (MG2), some  
206 inconsistencies remain, including gamma distribution shape parameters for hydrometeor size distributions and  
207 hydrometeor vertical overlap assumptions (J. Wang et al., 2021). Next-generation E3SM development includes efforts  
208 to improve agreement in the subgrid variability and microphysical assumptions involved in forward simulating  
209 satellite retrievals. Other issues include the simplified treatment of satellite cloud detection in simulators. For example,  
210 the CloudSat Cloud Profiling Radar (CPR) cloud mask value threshold  $\geq 30$  is applied for cloud detection in the  
211 WRDs’ A-Train analysis to indicate “good” or “strong” echo with high confidence detection (see next section and  
212 Supplement Table 1). The CPR cloud mask confidence levels consider signal-to-noise ratios, horizontal averaging,  
213 and spatial continuity (Marchand et al., 2008), but as this cloud mask is not available in COSPv2.0, CloudSat cloud  
214 detection is simulated by applying a reflectivity threshold  $-30 \leq Z_e \leq 20$  dBZ.

215 The WRDs rely on COSPv2.0 simulated MODIS and CloudSat retrievals. The WRDs in COSPv2.0 work as  
216 follows: First, COSPv2.0 takes in model atmospheric state and cloud variables including temperature, pressure,  
217 water vapor and hydrometeor mass mixing ratios, hydrometeor  $R_e$ , large-scale stratiform cloud fraction, convective  
218 cloud fraction and precipitation rate. The COSPv2.0 subcolumn generator SCOPS then produces subgrid

Formatted: Left



219 distributions of clouds and precipitation for better comparison with smaller scale satellite pixel measurements.

220 SCOPS subcolumns are homogenous, discrete samples generated such that a sufficiently large ensemble reproduces

221 the model column profile of bulk cloud properties (Webb et al., 2001; Swales et al., 2018). SCOPS assigns each

222 subcolumn a type (large-scale stratiform, convective or clear-sky) according to the host model’s convective and

223 large-scale stratiform cloud fraction. Cloud properties such as hydrometeor mass mixing ratios and  $R_e$  are distributed

224 homogeneously across the subcolumns by cloud type (i.e., all stratiform cloud subcolumns are assigned the same

225 stratiform ice and liquid mixing ratios as SCOPS only takes total convective and stratiform cloud fraction as input,

226 and does not consider stratiform liquid and ice cloud fraction in its default configuration. “Maximum-random”

227 cloud overlap is applied to subcolumns, consistent with the model parameterizations. The MODIS and CloudSat

228 simulators apply simplified versions of their respective retrieval algorithms to each subcolumn, emulating MODIS

229 retrievals of cloud properties, radar reflectivity and lidar backscatter, respectively. Gridbox-mean values are

230 estimated from accumulated subcolumn statistics. The WRDs take as inputs gridbox-mean simulated MODIS

231 retrievals of LWP, IWP, COT and  $R_e$ , as well as subcolumn CloudSat reflectivity profiles. The simulated MODIS

232 COT represents in-cloud mean, as do the other MODIS variables used in the WRDs (e.g., LWP,  $R_e$ ). For example,

233 the MODIS liquid COT is computed by averaging the MODIS liquid COT in cloudy subcolumns across the grid-

234 box. In E3SMv2-COSP, the same in-cloud stratiform COT value from the E3SMv2 radiative transfer module is

235 distributed across all the subcolumns designated as stratiform cloud by SCOPS, as described above. These values

236 and cloud/clear-sky designations for each subcolumn are used as input to the MODIS simulator to calculate the in-

237 cloud MODIS liquid COT. Subcolumn-level SLWC reflectivity profiles are used as input to the WRDs, also with

238 cloud properties homogeneously distributed across the subcolumns of a given classification. Thus, in E3SM-COSP,

239 the SLWC samples within a gridbox that have the same subcolumn classification (i.e., stratiform liquid or stratiform

240 rain), will have the same simulated MODIS COT and CloudSat reflectivity profile.

241 Deviations from the original WRDs implemented in COSPv2.0 (Michibata et al., 2019b) include the application of

242 the simulated CloudSat ground-clutter filter (available in COSPv2.0, but not applied to the WRDs previously) for

243 better comparison with CloudSat retrievals, and the elimination of the “fracout” input used in the SLWC detection

244 scheme from SCOPS. “Fracout” is the subcolumn-level cloud classification by vertical level from SCOPS, where each

245 level of each subcolumn is designated as large-scale stratiform, convective, or clear-sky. This input was removed from

246 the WRDs’ SLWC detection algorithm because of the lack of comparable cloud-type designation in the observations

Formatted: Font: (Default) Times New Roman, 10 pt

Formatted: Font: (Default) Times New Roman, 10 pt

Formatted: Font: (Default) Times New Roman, 10 pt

Formatted: Font: (Default) Times New Roman, 10 pt

Formatted: Font: (Default) Times New Roman, 10 pt

Formatted: Font: (Default) Times New Roman, 10 pt

Formatted: Font: (Default) Times New Roman, 10 pt

Formatted: Font: (Default) Times New Roman, 10 pt

Formatted: Font: (Default) Times New Roman, 10 pt

Formatted: Font: (Default) Times New Roman, 10 pt

Formatted: Font: (Default) Calibri, 12 pt

247 and CloudSat simulator and because “fracout” vertical cloud profiles were observed to deviate significantly from  
248 CloudSat reflectivity profiles (i.e., fracout indicates clear-sky where CloudSat reflectivity indicates cloud, or vice  
249 versa).

### 250 2.3 Satellite data

251 The MOD06-1KM-AUX R05 product (Platnick et al., 2017), which provides MODIS collection 6 retrievals [at 1 km](#)  
252 [resolution](#) along the CloudSat footprint, supplied the 6 MODIS cloud retrievals required for the SLWC detection  
253 described in Suzuki et al. (2010): LWP, IWP,  $R_c$ , COT, cloud top pressure and cloud layer number. [Standard MODIS](#)  
254 [products from the 2.1  \$\mu\text{m}\$  channel were used for  \$R\_c\$ , consistent with the simulated MODIS  \$R\_c\$  used in the WRDs.](#)

Formatted: Subscript

255 Atmospheric temperature profiles were obtained from ECMWF-AUX R05 (Partain and Cronk, 2017), which includes  
256 temperature profiles from the European Centre for Medium-Range Weather Forecast (ECMWF) [model](#) (Dee et al.,  
257 2011) interpolated to the CloudSat footprint. 2B-GEOPROF R05 provided the CloudSat reflectivity profiles, the Cloud  
258 Profiling Radar (CPR) cloud mask and echo top characterization [at 1.8 km resolution](#) (Marchand et al., 2008). The  
259 detection of SLWCs and CFODD analysis in the present study follows Suzuki et al. (2010) (see Supplement Table 1  
260 for details) with one exception: a COT threshold was decreased from 15 to 0.3; this had a substantial impact on cloud  
261 occurrence (Figure 1; described next) and is consistent with the COT threshold implemented in the COSPv2.0 WRDs.  
262 [The decreased COT threshold also increases the weight of optically thin SLWCs, as the linear regression is applied to](#)  
263 [the CFODD source data directly \(i.e., the ICOD and reflectivity profiles\).](#)

### 264 2.4 Autoconversion sensitivity experiments and ERFaci

265 The autoconversion parameterization in E3SMv2 is a modified Khairoutdinov & Kogan (2000) scheme (hereafter,  
266 KK2000), in which coefficients were updated in response to large uncertainties in different cloud regimes and to  
267 improve fidelity in climate simulations. The KK2000 autoconversion scheme is  $\frac{\delta q_r}{\delta t_{auto}} = A Q_c^\alpha N_d^\beta$ , where  $q_r$  is  
268 the rainwater mixing ratio,  $Q_c$  is the cloud water mixing ratio,  $N_d$  is the cloud droplet number concentration, and  $A$ ,  $\alpha$   
269 and  $\beta$  are the modified coefficients.

270 To develop a constraint on the ERFaci due to autoconversion, we performed multiple pairs of simulations featuring  
271 preindustrial (PI) and present-day (PD) aerosol emissions. In each pair of simulations, one of the three coefficients  
272 ( $A$ ,  $\alpha$  or  $\beta$ ) was modified to its KK2000 value, a value reported by Wood (2005), [a value from Kogan \(2013\)](#)—or a

273 value within a range bounded by the three studies. [The Kogan \(2013\) coefficient values were derived from a large-](#)  
274 [eddy simulation \(LES\) with bin resolved microphysics for cumulus clouds, whereas the focus of Wood \(2005\) and](#)  
275 [KK2000 was stratocumulus clouds from observational and LES perspectives, respectively.](#) One additional experiment  
276 on the KK2000 parameterization for the accretion rate was performed, the formulation of which is  $\frac{\delta q_r}{\delta t_{accre}} =$   
277  $F_1 F_2 67 (Q_c Q_r)^{1.15} \rho^{-1.3}$ , where  $Q_r$  is the rain water mixing ratio,  $F_1$  represents subgrid  $Q_c$  variability,  $\rho$  is air density,  
278 and  $F_2$  is an accretion rate enhancement factor.  $F_2$  was increased by a factor of  $\sim 3$  in the accretion sensitivity  
279 experiment.  $F_2$  is considered a tunable parameter in E3SM (Ma et al., 2022). The experiment details are provided in  
280 Table 1.

281 Table 1. KK2000 coefficient and accretion enhancement factor values applied in 12 sensitivity experiments. Dash (“-”  
282 “) indicates the coefficient value was unchanged from the default E3SMv2 parameterization (equal to the “CNTL”  
283 simulation value).

Name	A	$\alpha$	$\beta$	accre
CNTL	3.05E4	3.19	-1.4	1.75
alpha01	-	4.22	-	-
beta01	-	-	-1.0	-
acoef100x	3.05E6	-	-	-
alpha02	-	2.47	-	-
acoef0.05x	1.35E3	-	-	-
alpha03	-	3.00	-	-
beta03	-	-	-1.79	-
beta04	-	-	-3.01	-
acoef10x	3.05E5	-	-	-
acoef5x	1.53E5	-	-	-
acoef50x	1.53E6	-	-	-
accre01	-	-	-	5

284

285 ERFaci for each pair of simulations was calculated following the Ghan (2013) method, where  $ERFaci = \Delta(F_{clean} -$   
286  $F_{clear, clean})$ .  $F_{clean}$  is the radiative flux at the top-of-atmosphere (TOA) neglecting the absorption and scattering of  
287 aerosols, and  $F_{clear, clean}$  is the radiative flux at the TOA neglecting both clouds and the absorption and scattering of  
288 aerosols. The  $\Delta$  indicates the PD – PI difference. While the PD-PI approach is a common strategy for estimating  
289 ERFaci, Christensen et al. (2023) demonstrated that it may yield a different estimate than the PD approach, where  
290 components of ERFaci (LWP adjustment,  $N_d$  adjustment, cloud fraction adjustment) are estimated by regressions of  
291 cloud properties multiplied by the anthropogenic aerosol fraction. We calculate ERFaci for SLWCs only, binned by  
292 the MODIS  $R_e$  range corresponding to the CFODD analysis.

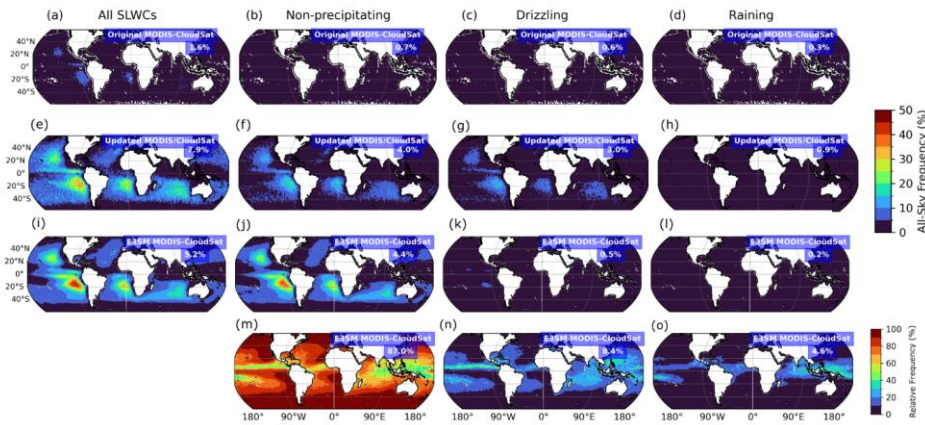
293 A constraint on  $ERFaci_{sw}$  was calculated from the linear regression between E3SMv2 CFODD slopes and  $ERFaci_{sw}$ ,  
294 using the MODIS-CloudSat CFODD slope as a reference. A 95% confidence interval for the linear fit was estimated  
295 by bootstrapping the linear regression within the uncertainty of the CFODD slopes. CFODD slope values were  
296 randomly sampled 1000 times within their 1-sigma error and repeatedly regressed with  $ERFaci_{sw}$ . The original data  
297 (i.e., RANSAC CFODD slope values and corresponding  $ERFaci_{sw}$  values) were additionally resampled with  
298 replacement to generate a distribution of coefficients for the ordinary least squares (OLS) regression. The 95%  
299 confidence interval for the linear fit was then calculated from the combined linear regression coefficient distributions  
300 to reflect uncertainty from both the OLS fit and the CFODD slopes.

### 301 **3 Updates to MODIS and CloudSat SLWC analysis and reference data**

302 The first diagnostic in the original WRDs featured relative frequencies of SLWCs by precipitation intensity in both  
303 the A-Train reference data and the COSPv2.0 output (e.g., Fig. 1 m-o). We have updated this diagnostic with all-sky  
304 frequencies and by decreasing the lower MODIS COT threshold from 15 to 0.3, for consistency with the WRDs  
305 implemented in COSPv2.0 (Fig. 1 a-l). SLWCs featured in Fig. 1 and all following figures and analyses are ocean-  
306 only due to higher uncertainties in MODIS retrievals over land (Platnick et al., 2017).

Formatted: Subscript

Formatted: Subscript



307  
 308 **Figure 1.** All-sky frequencies of total SLWCs June 2006 – Apr 2011, non-precipitating ( $Z_{max} < -15 \text{ dBZ}_e$ ), drizzling  
 309 ( $-15 \text{ dBZ}_e \leq Z_{max} < 0 \text{ dBZ}_e$ ) and raining ( $Z_{max} \geq 0 \text{ dBZ}_e$ ) ocean-only SLWCs according to original reference analysis of  
 310 MODIS and CloudSat observations (Michibata et al., 2019a, 2019b) (a-d), updated reference MODIS and CloudSat analysis (e-h)  
 311 and E3SMv2-COSPv2.0 (i-l). Figures m-o show frequencies of non-precipitating, drizzling and raining SLWCs relative to the total  
 312 SLWCs simulated by E3SMv2. Values in blue boxes indicate global ocean-only grid-weighted mean frequency. SLWCs were  
 313 undersampled in original reference A-Train analysis by a factor of  $\sim 5$ . Compared to the original reference A-Train data, the updated  
 314 analysis demonstrates that E3SM underrepresents rather than overrepresents total SLWC frequency and that precipitating SLWCs  
 315 are underrepresented by a factor of 6 compared to observations.

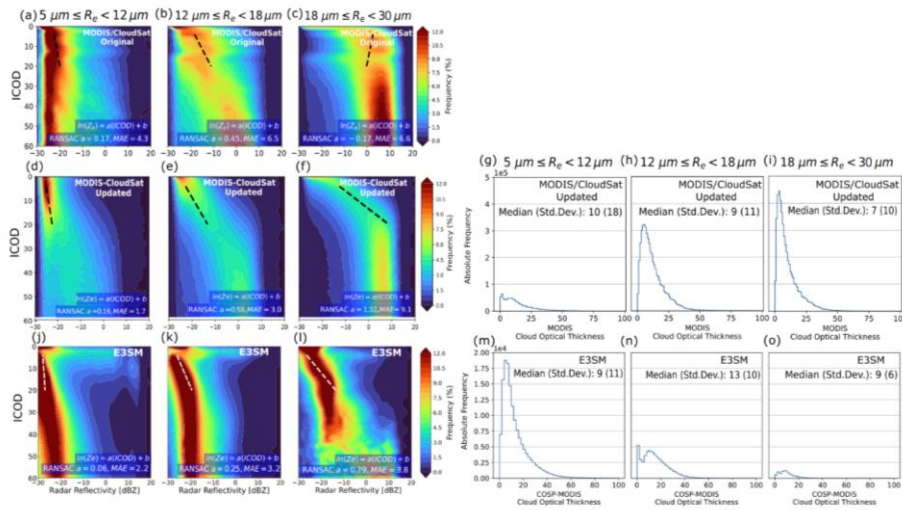
316 Figure 1 also shows that decreasing the lower MODIS COT threshold from 15 to 0.3 in the updated A-Train analysis  
 317 (Sect. 2.3) increased total SLWC sampling by 5-fold (global ocean mean, see Sect. 2.3) compared to the original  
 318 CFODD analysis in Michibata et al. (2019a) and Michibata et al. (2019b). The increase in SLWC sampling in the  
 319 reference data affects multiple outcomes of the model evaluation in this case: E3SMv2 underrepresents, rather than  
 320 overrepresents, total SLWCs, and the SLWCs that are missing from E3SMv2 are entirely the precipitating SLWC  
 321 populations. The underrepresentation of precipitating SLWCs in E3SMv2-COSP indicates that any bias from SCOPS  
 322 towards increased precipitation in warm liquid clouds is relatively minor (Sect. 2.2; Song et al. (2018)). Not all the  
 323 differences between the original and updated reference data can be explained by the change in COT threshold,  
 324 however, as we were unable to reproduce the original CFODD data with the updated satellite products used in this  
 325 study. Fig. S1 and S2 show that increasing the lower COT threshold from 0.3 to 15 yields SLWC frequencies that are

326 much closer to the original reference data (+25%) than the updated reference data, but significant differences remain  
327 in the CFODDs.

328 The effects of the increased SLWC sampling in the A-Train reference data also significantly affected the CFODDs  
329 and thus the comparison between A-Train and E3SMv2 droplet collection efficiencies. Figure 2 shows CloudSat  
330 reflectivity frequency binned by ICOD for the original A-Train reference data (Fig. 2 a-c), the updated A-Train  
331 reference data (d-f) and E3SMv2 (j-l), and RANSAC robust linear regression slopes at  $4 \leq \text{ICOD} \leq 20$ . In comparisons  
332 with various other linear regression techniques, we found that RANSAC best supported the comparison of CFODD  
333 slopes between E3SMv2 and observations because of the right-skewed distribution of CloudSat reflectivities at  $0 \leq$   
334  $\text{ICOD} \leq 20$  in E3SMv2 CFODDs (Figs. 2 j-l). RANSAC minimizes the median absolute error (MAE) and is less  
335 sensitive to strong outliers in the dimension of the predicted variable ( $Z_e$  in this case) compared to other linear  
336 regression techniques.

337 The updated A-Train CFODD distributions are significantly different than the original CFODD distributions (2D-  
338 Kolmogorov-Smirnov test,  $p \ll 0.05$ ). Compared to updated A-Train CFODDs, the E3SMv2 CFODDs show  
339 decreased droplet collection efficiencies and an increased range of reflectivities near the cloud top in all size bins,  
340 indicating that regardless of  $R_e$ , SLWCs are drizzling and raining near the cloud top with significantly higher frequency  
341 than SLWCs in observations but have decreased collection efficiency below cloud top compared to MODIS-CloudSat.

342



343

344 **Figure 2.** Contoured frequency by optical depth diagrams (CFODDs) for SLWCs June 2006 – April 2011 binned by MODIS cloud  
 345 top effective radius ( $R_e$ ) from original reference MODIS-CloudSat observations analysis (a-c), updated reference MODIS-CloudSat  
 346 observations analysis (d-f), and E3SMv2 (j-l). Random Sample Consensus (RANSAC) linear regressions were applied to the  
 347 CFODD at  $4 \leq \text{ICOD} \leq 20$  to estimate droplet collection efficiencies. RANSAC slopes and Median Absolute Error (MAE) values  
 348 are shown in blue boxes. Droplet collection efficiencies increase with MODIS  $R_e$  as expected, except for the largest  $R_e$  size bin in  
 349 the original reference data (Fig. s2c). Figs. g-i and m-o show absolute frequencies of SLWCs by MODIS COT, demonstrating that  
 350 E3SMv2 overrepresents SLWCs with small  $R_e$  relative to medium and large  $R_e$ , compared to observations.

351 The high reflectivities near the cloud top are pronounced in the subset of E3SMv2 SLWCs with  $4 < \text{MODIS COT} <$   
 352  $20$  (Fig. S3), indicating that the high reflectivity at low ICOD in Figs. 2 (j-l) is not just a product of a subset of  
 353 precipitating highly reflective, optically thin SLWCs, but that layers near the cloud top in deeper SLWCs are also  
 354 precipitating, high reflectivities near cloud top within optically thicker SLWCs also contribute to this strange feature  
 355 in the CFODD. The reflectivity profiles used to generate the CFODD come from the CloudSat simulator, which was  
 356 not modified for this study. Examples of simulated CloudSat reflectivity profiles in SLWCs with  $Z_e > 0$  dBZ near  
 357 cloud top are shown in Fig. S4. The source of this issue and its implications for E3SMv2 representation of liquid  
 358 cloud properties warrant further investigation that is beyond the scope of the present study.

359 ~~Figure 2 shows a~~Absolute frequencies of SLWCs binned by MODIS COT ~~infor~~ each CFODD  $R_e$  bin ~~are shown~~ for  
360 the updated A-Train analysis (Fig. 2 g-i) and E3SMv2 only (Fig. 2 m-o). Note, this information was unavailable in  
361 the original reference data (Michibata et al., 2019a). Compared to COT distributions in the updated A-Train analysis,  
362 E3SMv2 shows decreasing SLWC frequency with  $R_e$  and an underrepresentation of SLWCs with large  $R_e$ , which  
363 aligns with the underrepresentation of precipitating SLWCs in Fig. 1. Fig. 2o also shows that few SLWCs with large  
364  $R_e$  have a COT > 20, indicating that the CFODD reflectivity profile in Fig. 2l at ICOD > 20 is comprised of few  
365 samples. The SLWC COT PDFs have been implemented in the WRDs to support the interpretation of CFODD  
366 statistics.

## 367 4 Results and Discussion

### 368 4.1 CFODD analysis to constrain ERFaci due to warm rain processes

369 To demonstrate the potential of the CFODD analysis described above for constraining ERFaci<sub>sw</sub> due to warm rain  
370 processes, we performed 12 experiments featuring variations of E3SMv2's autoconversion and accretion  
371 parameterizations, computing ERFaci<sub>sw</sub> ~~for the SLWC samples represented in each CFODD and the corresponding~~  
372  ~~$R_e$  bin (hereafter, "ERFaci<sub>sw SLWCs</sub>")~~ following Ghan (2013; see Sect. 2.4). In each experiment, a single coefficient of  
373 either the KK2000 autoconversion or accretion parameterization was perturbed, each of which is treated as a tunable  
374 parameter in E3SMv2. The uncertain KK2000 coefficients, coupled with parameterization simplifications (e.g., bulk  
375 moments and assumed droplet size distributions), result in uncertainties and biases in the model representation of  
376 raindrop formation and growth. The experiments are described in Table 1, and the CFODDs for each experiment are  
377 shown in Fig. S5.

378 Figure 3 shows a strong negative correlation between E3SMv2 ERFaci<sub>sw SLWCs</sub> ~~and the~~with "small" or "medium"  $R_e$   
379 ~~(i.e.,  $5 \leq R_e < 18 \mu\text{m}$ ) and the -corresponding combined "small" and "medium"  $R_e$   $5 \leq R_e < 18 \mu\text{m}$  CFODD slope ( $5 \leq$   
380  ~~$R_e < 18 \mu\text{m}$ , Pearson's  $R = -0.91$ ). SLWCs with large  $R_e$  ( $18 \leq R_e < 30 \mu\text{m}$ ) were excluded from the analysis in Fig.~~  
381 3 because this population represents a negligible fraction of total SLWCs in E3SMv2 (see Fig. S6), resulting in poor  
382 sampling statistics and larger regression uncertainties. ~~The correlation between ERFaci<sub>sw</sub> and CFODD slope is~~  
383 ~~stronger in the combined CFODDs relative to the CFODDs considered separately (Fig. S7, also see discussion below).~~  
384 ~~As CFODD slopes represent an estimate of droplet collection efficiency, Fig. 3 indicates that ERFaci<sub>sw</sub> strengthens~~  
385 ~~(increases in magnitude) with increasing droplet collection efficiency in E3SMv2 SLWCs with  $R_e$  between 5 and 18~~~~

Formatted: Subscript

Formatted: Subscript

Formatted: Subscript

Formatted: Subscript



386 ~~μm.~~ As CFODD slopes represent an estimate of droplet collection efficiency, Fig. 3 ~~indicates~~ demonstrates that  
387  $ER_{faci_{sw}}$  strengthens (increases in magnitude) with increasing droplet collection efficiency in E3SMv2 SLWCs with  
388  $R_e$  between 5 and 18 μm. One possible physical explanation for the relationship between autoconversion, droplet  
389 collection efficiency, and  $ER_{faci_{sw}}$  is that increased autoconversion rates increase the susceptibility of clouds to  
390 precipitation suppression by aerosols. For a given optical depth, SLWCs with lower LWP and/or higher  $N_d$  will  
391 precipitate more when the autoconversion rate is increased. A larger population of precipitating SLWCs results in  
392 increased susceptibility to precipitation suppression by aerosols overall. When aerosols suppress precipitation (e.g.,  
393 Suzuki et al., 2013), LWP and/or cloud fraction may be enhanced, resulting in brighter clouds and stronger  $ER_{faci_{sw}}$ .  
394 The relationship between aerosols, LWP and cloud fraction (Albrecht, 1989), however, is highly uncertain, varies  
395 regionally (Sato et al., 2018), and is influenced by processes that are buffered over multiple spatiotemporal scales  
396 (Stevens and Feingold, 2009). Additionally, E3SMv2's CFODD slope ("CNTL" simulation) agrees with MODIS-  
397 CloudSat within uncertainty, indicating that droplet collection efficiency is well-represented according to CFODD  
398 analysis.

399

400

401

402

Formatted: Font: (Default) Times New Roman, 10 pt

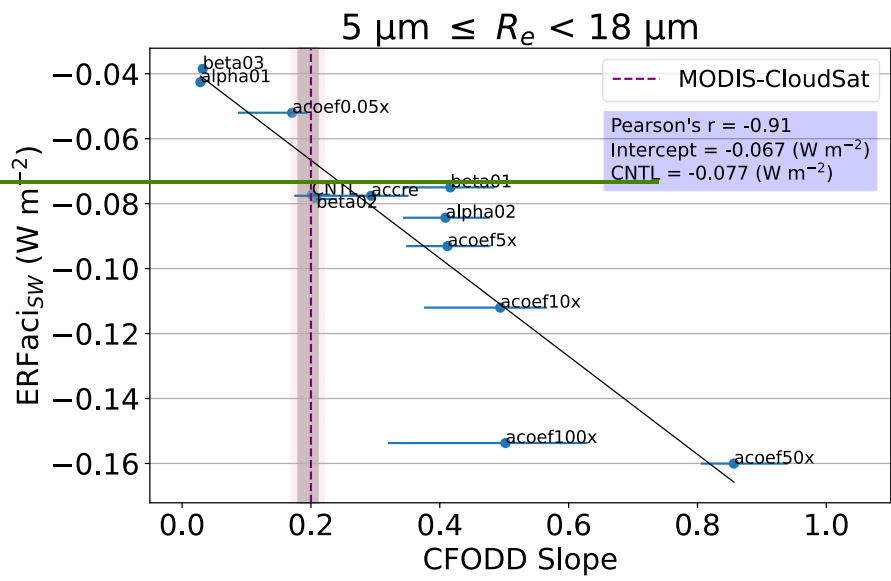
Formatted: Font: (Default) Times New Roman, 10 pt, Subscript

Formatted: Font: (Default) Times New Roman, 10 pt

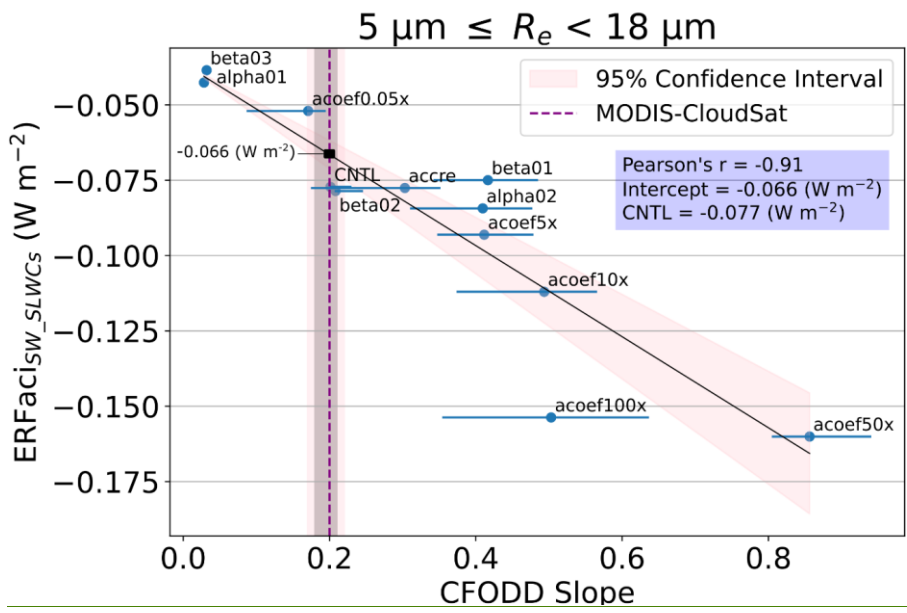
Formatted: Font: (Default) Times New Roman, 10 pt

Formatted: Font: 10 pt

Formatted: Line spacing: Double



403



404

405 **Figure 3.** Linear regression between E3SMv2  $ERFac_{iSW\_SLWCs}$  and CFODD slopes, generated from SLWCs with MODIS  $R_e$   
 406 between 5 and 18  $\mu m$ , in 12 PD autoconversion and accretion sensitivity experiments.  $ERFac_{iSW\_SLWCs}$  values reflect the SLWCs  
 407 represented in the corresponding CFODD (i.e., with  $R_e$  corresponding to the CFODD  $R_e$  bin). Results show a strong negative  
 408 correlation between E3SMv2  $ERFac_{iSW\_SLWCs}$  and CFODD slopes. We constrain the  $ERFac_{iSW}$  by predicting the  
 409  $ERFac_{iSW\_SLWCs}$  value at the reference MODIS-CloudSat  $5 \leq R_e < 18 \mu m$  CFODD slope (purple dashed line) from the  
 410 linear regression (intercept shown in blue box). The constrained  $ERFac_{iSW}$  value is decreased by  $143 \pm 6\%$  in magnitude compared  
 411 to the CNTL simulation. Error bars represent 1-sigma error estimated from RANSAC-fit bootstrapping (Sect. 2). Grey and pink  
 412 shaded regions indicate the 68 and 95% confidence intervals for the MODIS-CloudSat CFODD slope, respectively. Labels  
 413 indicate the sensitivity experiment names (Table 1).

414 In Figure 3, we constrain  $ERFac_{iSW}$  due to autoconversion uncertainties using the linear regression between the  
 415 simulated CFODD slopes and  $ERFac_{iSW\_SLWCs}$ .  $ERFac_{iSW}$  and  $ERFac_{iSW\_SLWCs}$  values were calculated following Ghan  
 416 et al. (2013), which considers the difference in TOA radiative flux between the PD and PI experiments, neglecting  
 417 direct forcing of aerosols (see Sect. 2.4 for details). We estimated the constrained value of  $ERFac_{iSW\_SLWCs}$  at the  
 418 intercept of the linear relationship with in Fig. 3 and the observed MODIS-CloudSat CFODD slope (Fig. S84), as a  
 419 reference. The  $ERFac_{iSW\_SLWCs}$  predicted by the linear regression at the MODIS-CloudSat slope value is  $-0.0667 W$   
 420  $m^{-2}$ , a  $143 \pm 6\%$  decrease in magnitude compared to the  $ERFac_{iSW\_SLWCs}$  value predicted by the E3SMv2 CNTL  
 421 simulation ( $-0.077 W m^{-2}$ ). E3SMv2's total  $ERFac$  ( $-1.50 W m^{-2}$ ), inclusive of all cloud types and the longwave forcing  
 422 component, falls within the IPCC AR6 'very likely' range for  $ERFac$  ( $-1.0 \pm 0.7 W m^{-2}$ ). The shortwave component  
 423 of  $ERFac$  is significantly larger than longwave in CMIP6 models (e.g., multimodel means of  $-0.91$  and  $+0.10 W m^{-2}$ ,  
 424 respectively, as reported in Smith et al. 2020). Thus, but our results indicate that correcting for eliminated the bias in  
 425  $ERFac_{iSW}$  due to autoconversion uncertainties -would decrease the magnitude of  $ERFac_{iSW}$  and bring the predicted  
 426 total  $ERFac$  closer to the median IPCC  $ERFac$  value (Forster et al., 2021).

Formatted: Subscript

Formatted: Subscript

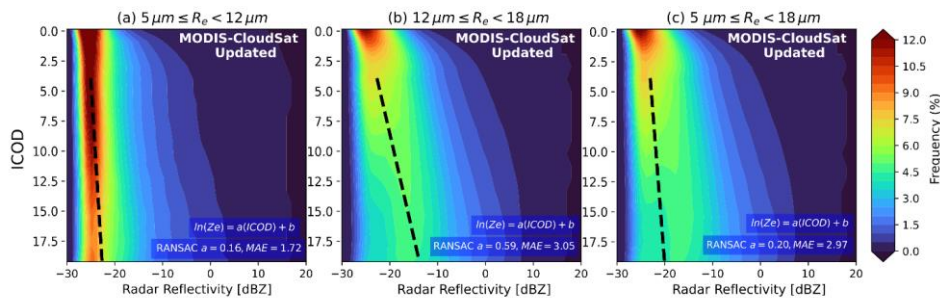
Formatted: Not Superscript/ Subscript

Formatted: Subscript

Formatted: Subscript

Formatted: Font: (Default) Times New Roman, 10 pt

Formatted: Font: (Default) Times New Roman, 10 pt



427

428 **Figure 4.** CFODDs for subset of SLWCs with max CloudSat reflectivity < 20 dBZ and COT < 20, June 2006 – April 2011, binned  
 429 by MODIS  $R_e$  from updated reference MODIS-CloudSat observations analysis (a-b), and with combined “small” and “medium”  
 430  $R_e$  SLWCs in (c). RANSAC linear regressions were applied to the CFODD at  $4 < \text{ICOD} < 20$  to estimate droplet collection  
 431 efficiencies. RANSAC slopes and Median Absolute Error (MAE) values are shown in blue boxes.

Formatted: Font: 9 pt, Bold

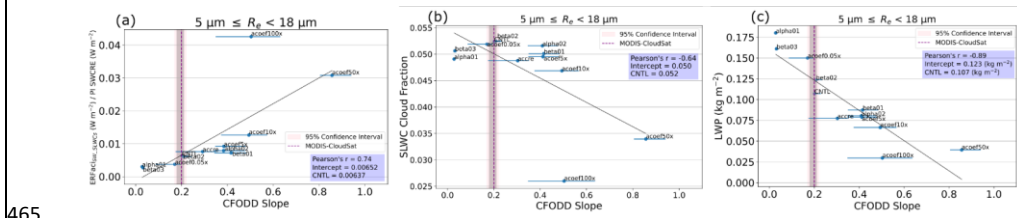
432 As  $ER_{\text{Faci}_{\text{SW}}}$  is the result of many cloud processes, the updated CFODD analysis should be interpreted as a constraint  
 433 on the component of  $ER_{\text{Faci}_{\text{SW}}}$  that is modulated by droplet collection efficiency due to autoconversion. In other  
 434 words, the updated CFODD analysis shows the change in  $ER_{\text{Faci}_{\text{SW}}}$  one would expect if the bias in  $ER_{\text{Faci}_{\text{SW}}}$  due to  
 435 a specific process representation affecting droplet collection efficiency were eliminated. Base cloud processes that are  
 436 independent of aerosol also contribute significantly to  $ER_{\text{Faci}}$  estimates (Mülmenstädt et al., 2020). Autoconversion  
 437 perturbations affect base cloud state (e.g., LWP, cloud fraction) and could, for example, cause stronger  $ER_{\text{Faci}}$  by  
 438 increasing cloud amount rather than increasing the impact of ACI on SW radiative forcing. Jing et al. (2019) evaluated  
 439 different autoconversion parameterization schemes in an ESM using the CFODD analysis described in Michibata et  
 440 al. (2019b) and found that the autoconversion scheme that yielded the best warm rain representation predicted a  
 441 significantly stronger  $ER_{\text{Faci}}$  that exceeded the uncertainty range of the IPCC AR5 and canceled out much of the  
 442 warming trend of the last century. The conflict between process representation and  $ER_{\text{Faci}}$  predictions in Jing et al.  
 443 (2019) underscore a challenge with process-based constraints: improving the representation of a process can result in  
 444 adverse outcomes to climate prediction due to compensating biases in the model. This challenge is particularly  
 445 troublesome for constraints on processes like autoconversion that affect the base cloud state because decreasing  
 446 autoconversion rates can increase total cloud amount, which can yield stronger  $ER_{\text{Faci}}$ . Thus, a decreased  
 447 autoconversion rate may improve precipitation outcomes in an ESM that presents the common “too frequent” warm  
 448 rain bias (e.g., Stephens et al., 2010), yet cause improbably strong  $ER_{\text{Faci}}$ . Our results show, however, that decreased

Formatted: Font: 9 pt, Bold

449 autoconversion rates result in weaker  $ERFac_{sw\_SLWCs}$  (Fig. 3), demonstrating that the base cloud state issue presented  
 450 in prior studies of autoconversion is not a dominant factor contributing to the  $ERFac_{sw}$  of warm rain processes in  
 451 E3SMv2.

Formatted: Subscript

452 Fig. S9ure 5a shows the linear relationship between  $ERFac_{sw\_SLWCs}$  normalized by the PI SW Cloud Radiative Effect  
 453 (SWCRE), which represents the fraction of  $ERFac$  that is independent of base cloud state changes, and CFODD slope.  
 454 The correlation coefficient in Fig. S7-5a (Pearson's  $R = 0.74$ ) is decreased compared to Fig. 3 (Pearson's  $R = -0.91$ ).  
 455 However, comparing the negative correlations between CFODD slope and PI SLWC cloud fraction (Fig. S405b;  
 456 Pearson's  $R = -0.64$ ) and LWP (Fig. S445c; Pearson's  $R = -0.89$ ) with Fig. 3, the  $ERFac_{sw\_SLWCs}$  increases in  
 457 magnitude as LWP and cloud fraction decrease, further demonstrating that the contribution of base cloud state to  
 458  $ERFac_{sw\_SLWCs}$  is relatively minor. The decreased correlation coefficient in Fig. S6-5a could also be influenced by  
 459 poor sampling statistics in the "acoef100x" experiment. The acoef100x was the only one of six experiments involving  
 460 perturbations of the "A" coefficient in KK2000 (Table 1; Sect. 2.4) in which the CFODD slope did not increase with  
 461 an increase in magnitude of the "A" coefficient. Given the significant decrease in SLWC cloud fraction in this  
 462 experiment compared to the others (Fig. S405b, Table S2), the CFODD slope result may be affected by insufficient  
 463 sample size, an additional uncertainty of the CFODD linear regression that is not reflected in the bootstrapping-based  
 464 uncertainty estimate (Sect. 2).



465 **Figure 5.** Linear regression between (a) E3SMv2  $ERFac_{sw\_SLWCs}$  normalized by SWCRE, (b) SLWC cloud fraction, (c) SLWC  
 466 LWP and CFODD slopes in 12 PD autoconversion and accretion sensitivity experiments, calculated for SLWCs with MODIS  $R_e$   
 467 between 5 and 18  $\mu m$ .  $ERFac_{sw\_SLWCs}$  values reflect the SLWCs represented in the corresponding CFODD (i.e., with  $R_e$   
 468 corresponding to  $5 < R_e < 18 \mu m$ ). Error bars represent 1-sigma error estimated from RANSAC-fit bootstrapping (Sect. 2). Grey  
 469 and pink shaded regions indicate the 68 and 95% confidence intervals for the MODIS-CloudSat CFODD slope, respectively. Labels  
 470 indicate the sensitivity experiment names (Table 1).  
 471

Formatted: Font: 9 pt, Bold

Formatted: Font: 9 pt

472 While we derive a constraint for  $ERF_{Fac_{SW}}$  using the combined small and medium  $R_e$  CFODDs, when the  $R_e$  subsets  
473 are considered individually, they show distinct contributions to  $ERF_{Fac_{SW\_SLWCs}}$ . Fig. S7 shows that SLWCs with small  
474  $R_e$  have a negative  $ERF_{Fac_{SW\_SLWCs}}$ , but that SLWCs in the medium and large  $R_e$  subsets have positive  $ERF_{Fac_{SW\_SLWCs}}$   
475 values. This indicates that the dominant effect of aerosols on shortwave radiative forcing in the medium and large  
476 SLWC subsets is decreased cloud fraction, which is reflected in the decreased SLWC sample sizes in the PD  
477 simulations compared to PI (Fig. S12S8, S13S9). The negative linear relationship between  $ERF_{Fac_{SW\_SLWCs}}$  and  
478 CFODD slope in the medium and large  $R_e$  subsets indicates that increasing droplet collection efficiency partially  
479 counteracts the decrease in cloud fraction due to aerosol. The small  $R_e$  SLWCs, however, show a positive correlation  
480 between  $ERF_{Fac_{SW}}$  and CFODD slope, indicating that  $ERF_{Fac_{SW}}$  weakens as autoconversion rates increase, likely due  
481 to decreased precipitation suppression susceptibility in this subset. The small  $R_e$  SLWCs, however, show a negative  
482 correlation between  $ERF_{Fac_{SW}}$  and CFODD slope, indicating that the dominant effect of aerosols on this subset via  
483 decreasing of the CFODD slope is to strengthen  $ERF_{Fac_{SW}}$ . The combined small and medium CFODD and  
484  $ERF_{Fac_{SW\_SLWCs}}$ , therefore, represent the convolution of two populations with differing  $ERF_{Fac_{SW}}$  sensitivities to  
485 autoconversion perturbations. We chose to constrain  $ERF_{Fac_{SW}}$  using the combined small and medium CFODD and  
486  $ERF_{Fac_{SW\_SLWCs}}$  due the correlation performance and the dearth of large  $R_e$  SLWCs in E3SMv2. However, constraints  
487 for  $ERF_{Fac_{SW}}$  could potentially be derived for each individual  $R_e$  subset or various combinations thereof, depending  
488 on the distribution of SLWCs among the  $R_e$  size bins and their contribution to the host model's  $ERF_{Fac}$ . Considering  
489 that constrained  $ERF_{Fac_{SW}}$  increases in magnitude with increasing  $R_e$  in Fig. S7 the underrepresentation of SLWCs  
490 with large  $R_e$  in E3SMv2 represents a compensating bias, without which the total  $ERF_{Fac}$  bias would be even larger  
491 compared to IPCC AR6.

#### 492 4.2 Limitations of CFODD-based constraint on $ERF_{Fac}$

493 There are multiple limitations to the CFODD analysis that should be considered in its application as a constraint for  
494  $ERF_{Fac}$ . First, droplet collection is not explicitly represented in ESMs with bulk microphysical schemes such as  
495 E3SMv2, –but is instead implicit in an amalgamation of process and drop size distribution parameterizations  
496 controlling the evolution of the cloud and precipitation. Delving into the impact of these individual processes on  
497 CFODD-based constraint of  $ERF_{Fac}$  is a good target of future work, while autoconversion modulation of  $ERF_{Fac}$  was  
498 the primary focus here. Furthermore, simulated radar reflectivity is highly sensitive to particle size distribution

Formatted: Font: (Default) Times New Roman, 10 pt

Formatted: Font: (Default) Times New Roman, 10 pt, Not Superscript/ Subscript

Formatted: Font: (Default) Times New Roman, 10 pt

Formatted: Font: Bold

499 assumptions in the forward simulator (e.g., Bodas-Salcedo et al., 2011; J. Wang et al., 2021). The host model,  
500 therefore, could represent warm rain microphysical processes with high fidelity but still produce biased CFODD  
501 profiles when compared with observations. In COSPv2.0, the CloudSat simulator calculates size distributions from  
502 an assumed distribution (e.g., log-normal, gamma, exponential) as well as mass-mixing ratios, precipitation fluxes,  
503 and gridbox-mean  $R_e$  from the host model. Default COSPv2.0 size distributions were used in this study: log-normal  
504 for large-scale stratiform and convective cloud liquid, and exponential for large-scale stratiform and convective cloud  
505 rain. The CFODD analysis itself is subject to multiple uncertainties, including the use of simple adiabatic and  
506 condensational growth assumptions to scale MODIS COT to ICOD. These assumptions result in a vertical distribution  
507 of optical depth, mass concentrations and particle size that may not reflect reality. For example, in the CFODD, particle  
508 size and mass concentration are assumed to monotonically increase with height, yet in the real cloud, particle sizes  
509 may decrease near the cloud top due to evaporation and entrainment (Suzuki et al., 2010). The uncertainties from  
510 assumed hydrometeor size distributions and CFODD construction should be carefully considered when using the  
511 CFODD to evaluate model droplet collection efficiencies against observations and in the application as an ERFaci  
512 constraint. Simulated reflectivity biases affect the evaluation of the model CFODD slope against the observational  
513 CFODD slope and thus affect the estimation of ERFaci bias.

514 A few additional limitations on CFODD analysis are imposed by biases in E3SMv2 SLWC representation. The ERFaci  
515 constraint is restricted to the small and medium  $R_e$  CFODDs because of the underrepresentation of SLWCs with large  
516  $R_e$ . SLWCs with medium  $R_e$  are also underrepresented in E3SMv2, further limiting the CFODD analysis of E3SMv2  
517 ERFaci because process perturbations are limited to the extent that they do not significantly reduce the number of  
518 SLWCs with medium  $R_e$ . The high reflectivity near cloud top at  $ICOD < 4$  in E3SMv2 CFODDs presents another  
519 limitation. SLWCs with  $COT < 4$  represent a significant fraction of the SLWC population in both A-Train and  
520 E3SMv2 (Fig. 2), so including optically thin SLWCs in the linear regression would likely affect the CFODD slope  
521 and droplet collection efficiency estimates.

522 Despite these limitations and the uncertainty associated with estimates of droplet collection efficiency from simulated  
523 radar reflectivity, CFODD analysis offers a highly desired process-oriented constraint on ERFaci due to warm rain  
524 processes. In E3SMv2, the CFODD slope exhibits the expected behavior in response to autoconversion perturbations:  
525 slope increases with perturbations that increase the autoconversion rate and decreases with perturbations that decrease

526 the autoconversion rate. Our results also show that the model  $ER_{Faci_{SW}}$  is highly sensitive to the processes that the  
527 CFODD represents, enabling the constraint of  $ER_{Faci_{SW}}$  against the CFODD slope derived from MODIS-CloudSat  
528 cloud retrievals. Prior studies have demonstrated that radar reflectivity biases can be partially mitigated by bringing  
529 the forward simulator into better agreement with the host model's microphysics parameterization and subgrid  
530 variability (Song et al., 2018b; J. Wang et al., 2021). Modified versions of COSP featuring improved consistency with  
531 E3SM are to be implemented in future E3SM model versions, which will decrease the uncertainties associated with  
532 CFODD analysis of E3SM.

### 533 **6.5 Summary**

534 In this study, we present an updated CFODD analysis and demonstrate how it can be applied to ESMs as a process-  
535 oriented constraint on  $ER_{Faci}$ . When E3SMv2's ~~droplet collection efficiency~~ CFODD slope is constrained by MODIS-  
536 CloudSat retrievals, E3SMv2's  $ER_{Faci_{SW}}$  is reduced by  $14.3 \pm 6\%$ . Demonstrated here as a constraint based on the  
537 component of  $ER_{Faci_{SW}}$  on that is modulated by autoconversion, CFODD analysis represents a highly desirable  
538 constraint on a process, circumventing the equifinality issue that bedevils atmospheric state variable-based approaches  
539 (Mülmenstädt et al., 2020). Limitations of CFODD-based constraint of  $ER_{Faci}$  include the implicit representation of  
540 droplet collection efficiency in many ESMs, including E3SMv2, the sensitivity of simulated radar reflectivity to  
541 droplet size distribution representations and simplifying assumptions applied to construct the CFODD (e.g., adiabatic-  
542 condensational growth). While this study focuses on autoconversion, future studies should apply CFODD analysis  
543 could potentially apply to any other microphysical processes ~~parameterization~~ that affects droplet collection efficiency  
544 (e.g., accretion, droplet breakup, evaporation) to generate additional  $ER_{Faci}$  constraints.

545 Several updates to the WRDs package in COSPv2.0 were made to support the application of CFODD analysis to  
546 ESMs. In addition to the original WRDs diagnostics featuring relative frequencies of SLWCs by precipitation intensity  
547 and the CFODD by  $R_e$ , we have implemented additional diagnostics in the WRDs that include all-sky SLWC  
548 frequency maps and MODIS SLWC COT distributions for CFODD sampling statistics. Other updates include the  
549 estimation of CFODD slopes using Random Sample Consensus robust linear regression and changes to the SLWC  
550 detection schemes for better comparison between observations and satellite simulators.

551 In addition to the modifications of the WRDs described above, the MODIS and CloudSat observational reference data  
552 has been updated for consistency with COSPv2.0 SLWC detection. SLWC detection is increased 5-fold in the updated

Formatted: Subscript



553 reference data. The increase in SLWC sampling also significantly affected the CFODD distributions and consequently,  
554 the A-Train reference droplet collection efficiency at large  $R_e$  ( $18 \mu\text{m} \leq R_e < 30 \mu\text{m}$ ). The updated WRDs showed that  
555 droplet collection efficiencies in E3SMv2 are decreased compared to observations and SLWCs with small MODIS  $R_e$   
556 ( $5 \mu\text{m} \geq R_e > 12 \mu\text{m}$ ) are overrepresented. The E3SMv2 CFODD results also show reflectivities exceeding 0 dBZ near  
557 cloud top at  $2 < \text{ICOD} < 4$  yet relatively low reflectivities at  $\text{ICOD} > 5$ . The unreasonably high reflectivities near cloud  
558 top may indicate artifacts due to inconsistencies between E3SMv2 outputs and COSPv2.0 inputs to the CloudSat  
559 simulator. This issue motivates further investigation in future studies involving applications of the CloudSat simulator  
560 to E3SM. The E3SMv2 CFODD results also show that simulated reflectivity profiles near the cloud top are decoupled  
561 from the cloud below.—The updates described herein have increased the WRDs’ utility for evaluating model warm  
562 rain process representation and support the analysis needed to derive a constraint on ERFaci from CFODD analysis.  
563 Through an evaluation of E3SMv2, we demonstrate that the updated WRDs illuminate specific biases in SLWC  
564 representation and provide contextual sampling statistics that are critical for interpreting CFODD results and thus, for  
565 future applications of this observational constraint on ERFaci.

Formatted: Font: (Default) Times New Roman, 10 pt

Formatted: Font: 10 pt

566  
567 *Code and Data Availability:* The CloudSat and MODIS data products are available from the CloudSat Data Processing  
568 Center at CIRA/Colorado State University (<https://www.cloudsat.cira.colostate.edu/>; last access: June 28, 2023). The  
569 reference A-Train data used in this study is available here: <https://doi.org/10.5281/zenodo.8384180>. The modified  
570 source code of COSPv2.0 is available here: <https://doi.org/10.5281/zenodo.8371120> and the E3SMv2 source code is  
571 available here: <https://github.com/E3SM-Project/E3SM> (last access: September 27, 2023). The python package for  
572 the two-dimensional Kolmogorov-Smirnov test applied in this study is available here  
573 (<https://github.com/syrte/ndtest/tree/master>; last access: June 28, 2023). The python package scikit-learn was used for  
574 robust linear regression analysis (<https://scikit-learn.org/stable/>; last access: June 28, 2023).

575 *Author contributions:* CMB led the project, developed the additional WRDs diagnostics in this study, performed the  
576 model simulations and wrote the manuscript. PLM provided critical project guidance and support for modeling and  
577 analysis. MWC led the A-Train observations analysis and provided guidance on additional WRDs diagnostics  
578 development. AV provided input on CFODD analysis applications. JM provided guidance on ERFaci analysis. TM  
579 and KS provided guidance on WRDs applications. All authors contributed to writing the manuscript.

580 *Competing Interests:* At least one of the (co-)authors is a member of the editorial board of Atmospheric Chemistry  
581 and Physics.

582 *Acknowledgements:* The study was supported as part of the Enabling Aerosol–cloud interactions at Global  
583 convection-permitting scales (EAGLES) project (project no. 74358) sponsored by the United States Department of  
584 Energy (DOE), Office of Science, Office of Biological and Environmental Research (BER), Earth System Model  
585 Development (ESMD) program area. The Pacific Northwest National Laboratory (PNNL) is operated for the DOE by  
586 the Battelle Memorial Institute under Contract DE-AC05-76RL01830. The research used high-performance  
587 computing resources from the PNNL Research Computing, the BER Earth System Modeling program's Compy  
588 computing cluster located at PNNL, and resources of the National Energy Research Scientific Computing Center  
589 (NERSC), a U.S. Department of Energy Office of Science User Facility located at Lawrence Berkeley National  
590 Laboratory, operated under Contract No. DE-AC02-05CH11231, using NERSC awards ALCC-ERCAP0025938 and  
591 BER-ERCAP0024471.

592 *Financial support.* This study was funded by the U.S. Department of Energy, Office of Science, Office of Biological  
593 and Environmental research, Earth System Model Development (ESMD) program area (project nos. 74358). KS and  
594 TM were supported by the Japan Society for the Promotion of Science KAKENHI (Grant JP19H05669), MEXT  
595 program for the Advanced Studies of Climate Change Projection (SENTAN) (Grant JPMXD0722680395), and the  
596 Environment Research and Technology Development Fund (S-20) (Grant JPMEERF21S12004) of the Environmental  
597 Restoration and Conservation Agency. TM was supported by the JST FOREST Program (Grant JPMJFR206Y),  
598 and the Japan Society for the Promotion of Science KAKENHI (Grant JP 23K13171).

599

600

## 601 **References**

602 Albrecht, B. A.: Aerosols, Cloud Microphysics, and Fractional Cloudiness, *Science*, 245, 1227–1230, PMID =  
603 17747885, 10.1126/science.245.4923.1227, 1989.

604

605 Bellouin, N., Quaas, J., Gryspeerdt, E., Kinne, S., Stier, P., Watson-Parris, D., Boucher, O., Carslaw, K. S.,  
606 Christensen, M., Daniau, A.-L., Dufresne, J.-L., Feingold, G., Fiedler, S., Forster, P., Gettelman, A.,  
607 Haywood, J. M., Lohmann, U., Malavelle, F., Mauritsen, T., ... Stevens, B.: Bounding Global Aerosol  
608 Radiative Forcing of Climate Change. *Rev. Geophys.*, 58(1), e2019RG000660,  
609 <https://doi.org/https://doi.org/10.1029/2019RG000660>, 2020.

610 Bogenschutz, P. A., Gettelman, A., Morrison, H., Larson, V. E., Craig, C., & Schanen, D. P.: Higher-Order  
611 Turbulence Closure and Its Impact on Climate Simulations in the Community Atmosphere Model. *J. Climate*,  
612 26(23), 9655–9676 <https://doi.org/https://doi.org/10.1175/JCLI-D-13-00075.1>, 2013.

613 Cesana, G., & Chepfer, H.: How well do climate models simulate cloud vertical structure? A comparison between  
614 CALIPSO-GOCCP satellite observations and CMIP5 models. *Geophys. Res. Lett.*, 39(20).  
615 <https://doi.org/https://doi.org/10.1029/2012GL053153>, 2012.

616 Christensen, M. W., Stephens, G. L., & Lebsock, M. D.: Exposing biases in retrieved low cloud properties from  
617 CloudSat: A guide for evaluating observations and climate data: *J. Geophys. Res.*, 118(21), 12, 112–120, 131.  
618 <https://doi.org/https://doi.org/10.1002/2013JD020224>, 2013.

619  
620 Dee, D. P., Uppala, S. M., Simmons, A. J., Berrisford, P., Poli, P., Kobayashi, S., Andrae, U., Balmaseda, M. A.,  
621 Balsamo, G., Bauer, P., Bechtold, P., Beljaars, A. C. M., van de Berg, L., Bidlot, J., Bormann, N., Delsol, C.,  
622 Dragani, R., Fuentes, M., Geer, A. J., Haimberger, L., Healy, S. B., Hersbach, H., Hólm, E. V., Isaksen, L.,  
623 Kållberg, P., Köhler, M., Matricardi, M., McNally, A. P., Monge-Sanz, B. M., Morcrette, J.-J., Park, B.-K.,  
624 Peubey, C., de Rosnay, P., Tavolato, C., Thépaut, J.-N., and Vitart, F.: The ERA-Interim reanalysis:  
625 configuration and performance of the data assimilation system, *Quarterly Journal of the Royal Meteorological*  
626 *Society*, 137, 553–597, <https://doi.org/10.1002/qj.828>, 2011.

627  
628 Gelaro, R., McCarty, W., Suárez, M. J., Todling, R., Molod, A., Takacs, L., Randles, C. A., Darmenov, A.,  
629 Bosilovich, M. G., Reichle, R., Wargan, K., Coy, L., Cullather, R., Draper, C., Akella, S., Buchard, V.,  
630 Conaty, A., da Silva, A. M., Gu, W., ... Zhao, B.: The Modern-Era Retrospective Analysis for Research and  
631 Applications, Version 2 (MERRA-2), *Journal of Climate*, 30(14), 5419–5454, <https://doi.org/10.1175/JCLI-D-16-0758.1>, 2017.

632  
633 Ghan, S. J.: Technical Note: Estimating aerosol effects on cloud radiative forcing, *Atmospheric Chemistry and*  
634 *Physics*, 13(19), 9971–9974. <https://doi.org/10.5194/acp-13-9971-2013>, 2013.

635 Golaz, J. C., Larson, V. E., & Cotton, W. R.: A PDF-based model for boundary layer clouds. Part I: Method and  
636 model description, *Journal of the Atmospheric Sciences*, 59(24), 3540–3551. [https://doi.org/10.1175/1520-0469\(2002\)059<3540:APBMFB>2.0.CO;2](https://doi.org/10.1175/1520-0469(2002)059<3540:APBMFB>2.0.CO;2), 2022.

637  
638 Golaz, J.-C., Van Roekel, L. P., Zheng, X., Roberts, A. F., Wolfe, J. D., Lin, W., Bradley, A. M., Tang, Q., Maltrud,  
639 M. E., Forsyth, R. M., Zhang, C., Zhou, T., Zhang, K., Zender, C. S., Wu, M., Wang, H., Turner, A. K., Singh,  
640 B., Richter, J. H., ... Bader, D. C.: The DOE E3SM Model Version 2: Overview of the Physical Model and  
641 Initial Model Evaluation. *Journal of Advances in Modeling Earth Systems*, 14(12), e2022MS003156.  
642 <https://doi.org/https://doi.org/10.1029/2022MS003156>, 2022.

643 Jing, X., Suzuki, K., Guo, H., Goto, D., Ogura, T., Koshiro, T., and Mülmenstädt, J.: A Multimodel Study on Warm  
644 Precipitation Biases in Global Models Compared to Satellite Observations, *Journal of Geophysical Research:*  
645 *Atmospheres*, 122, 11, 806–811, 824, <https://doi.org/10.1002/2017JD027310>, issue = 21, 2017.

646  
647 Jing, X., Suzuki, K., & Michibata, T.: The Key Role of Warm Rain Parameterization in Determining the Aerosol  
648 Indirect Effect in a Global Climate Model. *Journal of Climate*, 32(14), 4409–4430.  
649 <https://doi.org/https://doi.org/10.1175/JCLI-D-18-0789.1>, 2019.

650 Kay, J. E., Wall, C., Yettella, V., Medeiros, B., Hannay, C., Caldwell, P., & Bitz, C.: Global climate impacts of  
651 fixing the Southern Ocean shortwave radiation bias in the Community Earth System Model (CESM), *Journal*  
652 *of Climate*, 29(12), 4617–4636. <https://doi.org/10.1175/JCLI-D-15-0358.1>, 2016.

653 Khairoutdinov, M., & Kogan, Y. (2000). A New Cloud Physics Parameterization in a Large-Eddy Simulation Model  
654 of Marine Stratocumulus. *Monthly Weather Review*, 128(1), 229–243.  
655 [https://doi.org/https://doi.org/10.1175/1520-0493\(2000\)128<0229:ANCPPI>2.0.CO;2](https://doi.org/https://doi.org/10.1175/1520-0493(2000)128<0229:ANCPPI>2.0.CO;2)

Formatted: Font: (Default) Times New Roman, 10 pt

Formatted: Font: (Default) Times New Roman, 10 pt

Formatted: Font: (Default) Times New Roman, 10 pt

656 Kogan, Y.: A Cumulus Cloud Microphysics Parameterization for Cloud-Resolving Models, *Journal of the*  
657 *Atmospheric Sciences*, 70, 1423-1436, <https://doi.org/10.1175/JAS-D-12-0183.1>, 2013.

Formatted: Font: (Default) Times New Roman, 10 pt

658

Formatted: Font: (Default) Times New Roman, 10 pt

659 Larson, V. E.: CLUBB-SILHS: A parameterization of subgrid variability in the atmosphere,  
660 <http://arxiv.org/abs/1711.03675>, 2017.

Formatted: Font: (Default) Times New Roman, 10 pt

661 Larson, V. E., & Golaz, J.-C.: Using Probability Density Functions to Derive Consistent Closure Relationships  
662 among Higher-Order Moments. *Monthly Weather Review*, 133(4), 1023–1042.  
663 <https://doi.org/https://doi.org/10.1175/MWR2902.1>, 2005.

664 Liu, X., Easter, R. C., Ghan, S. J., Zaveri, R., Rasch, P., Shi, X., Lamarque, J. F., Gettelman, A., Morrison, H., Vitt,  
665 F., Conley, A., Park, S., Neale, R., Hannay, C., Ekman, A. M. L., Hess, P., Mahowald, N., Collins, W.,  
666 Iacono, M. J., ... Mitchell, D.: Toward a minimal representation of aerosols in climate models: Description  
667 and evaluation in the Community Atmosphere Model CAM5. *Geoscientific Model Development*, 5(3), 709–  
668 739. <https://doi.org/10.5194/GMD-5-709-2012>, 2012.

669 Liu, X., Ma, P.-L., Wang, H., Tilmes, S., Singh, B., Easter, R. C., Ghan, S. J., & Rasch, P. J. Description and  
670 evaluation of a new four-mode version of the Modal Aerosol Module (MAM4) within version 5.3 of the  
671 Community Atmosphere Model. *Geoscientific Model Development*, 9(2), 505–522,  
672 <https://doi.org/10.5194/gmd-9-505-2016>, 2016.

673 Mangla, R., Indu, J., & Lakshmi, V.: Evaluation of convective storms using spaceborne radars over the Indo-  
674 Gangetic Plains and western coast of India. *Meteorological Applications*, 27(3), e1917,  
675 <https://doi.org/https://doi.org/10.1002/met.1917>, 2020.

676 Marchand, R., Mace, G. G., Ackerman, T., & Stephens, G.: Hydrometeor Detection Using Cloudsat—An Earth-  
677 Orbiting 94-GHz Cloud Radar, *Journal of Atmospheric and Oceanic Technology*, 25(4), 519–533,  
678 <https://doi.org/10.1175/2007JTECHA1006.1>, 2008.

679 Michibata, T., Kawamoto, K., & Takemura, T.: The effects of aerosols on water cloud microphysics  
680 and macrophysics based on satellite-retrieved data over East Asia and the North Pacific, *Atmospheric*  
681 *Chemistry and Physics*, 14(21), 11935–11948, <https://doi.org/10.5194/acp-14-11935-2014>, 2014.

682 Michibata, T., Suzuki, K., Ogura, T., & Jing, X.: Data for the publication “Incorporation of inline warm rain  
683 diagnostics into the COSP2 satellite simulator for process-oriented model evaluation.” Zenodo,  
684 <https://doi.org/10.5281/zenodo.3370823>, 2019a.

685 Michibata, T., Suzuki, K., Ogura, T., & Jing, X.: Incorporation of inline warm rain diagnostics into the COSP2  
686 satellite simulator for process-oriented model evaluation. *Geoscientific Model Development*, 12(10), 4297–  
687 4307. <https://doi.org/10.5194/gmd-12-4297-2019>, 2019b.

688 Muhlbauer, A., McCoy, I. L., and Wood, R.: Climatology of stratocumulus cloud morphologies: Microphysical  
689 properties and radiative effects, *Atmos. Chem. Phys.*, 14, 2014.

Formatted: Font: (Default) Times New Roman, 10 pt

691 Mülmenstädt, J. and Feingold, G.: The Radiative Forcing of Aerosol–Cloud Interactions in Liquid Clouds: Wrestling  
692 and Embracing Uncertainty, *Current Climate Change Reports*, 4, 23-40, 10.1007/s40641-018-0089-y, 2018.

Formatted: Font: (Default) Times New Roman, 10 pt

693

694 Mülmenstädt, J., Nam, C., Salzmann, M., Kretschmar, J., L'Ecuyer, T. S., Lohmann, U., Ma, P.-L., Myhre, G.,  
695 Neubauer, D., Stier, P., Suzuki, K., Wang, M., & Quaas, J. (2020). Reducing the aerosol forcing uncertainty  
696 using observational constraints on warm rain processes. *Science Advances*, 6(22), eaaz6433.  
697 <https://doi.org/10.1126/sciadv.aaz6433>

698 Partain, P., & Cronk, H.: *CloudSat ECMWF-AUX auxiliary data product process description and interface control*  
699 *document*. California Institute of Technology Jet Propulsion Laboratory Doc., 15 pp.,

Formatted: Font: (Default) Times New Roman, 10 pt

Formatted: Font: (Default) Times New Roman, 10 pt

700 [https://www.cloudsat.cira.colostate.edu/cloudsat-static/info/dl/ecmwf-aux/ECMWF-](https://www.cloudsat.cira.colostate.edu/cloudsat-static/info/dl/ecmwf-aux/ECMWF-AUX_PDICD.P_R05.rev0_.pdf)  
701 [AUX\\_PDICD.P\\_R05.rev0\\_.pdf](https://www.cloudsat.cira.colostate.edu/cloudsat-static/info/dl/ecmwf-aux/ECMWF-AUX_PDICD.P_R05.rev0_.pdf), 2017, last access: 24 January 2024.

702 Platnick, S., Meyer, K. G., King, M. D., Wind, G., Amarasinghe, N., Marchant, B., Arnold, G. T., Zhang, Z.,  
703 Hubanks, P. A., Holz, R. E., Yang, P., Ridgway, W. L., & Riedi, J.: The MODIS Cloud Optical and  
704 Microphysical Products: Collection 6 Updates and Examples From Terra and Aqua. *IEEE Transactions on*  
705 *Geoscience and Remote Sensing*, 55(1), 502–525, <https://doi.org/10.1109/TGRS.2016.2610522>, 2017.

706 Rasch, P. J., Xie, S., Ma, P. L., Lin, W., Wang, H., Tang, Q., Burrows, S. M., Caldwell, P., Zhang, K., Easter, R. C.,  
707 Cameron-Smith, P., Singh, B., Wan, H., Golaz, J. C., Harrop, B. E., Roesler, E., Bacmeister, J., Larson, V. E.,  
708 Evans, K. J., ... Yang, Y.: An Overview of the Atmospheric Component of the Energy Exascale Earth System  
709 Model: *Journal of Advances in Modeling Earth Systems*, 11(8), 2377–2411.  
710 <https://doi.org/10.1029/2019MS001629>, 2019.

711 Sato, Y., Goto, D., Michibata, T., Suzuki, K., Takemura, T., Tomita, H., and Nakajima, T.: Aerosol effects on cloud  
712 water amounts were successfully simulated by a global cloud-system resolving model, *Nature Communications*,  
713 9, 985, 10.1038/s41467-018-03379-6, 2018.  
714

715 Smith, C. J., Kramer, R. J., Myhre, G., Alterskjær, K., Collins, W., Sima, A., Boucher, O., Dufresne, J.-L., Nabat, P.,  
716 Michou, M., Yukimoto, S., Cole, J., Paynter, D., Shiogama, H., O'Connor, F. M., Robertson, E., Wiltshire, A.,  
717 Andrews, T., Hannay, C., Miller, R., Nazarenko, L., Kirkevg, A., Olivié, D., Fiedler, S., Lewinschal, A.,  
718 Mackallah, C., Dix, M., Pincus, R., & Forster, P.: Effective radiative forcing and adjustments in CMIP6 models,  
719 *Atmospheric Chemistry and Physics*, 20, 9591–9618, 10.5194/acp-20-9591-2020, 2020.  
720

721 Song, H., Zhang, Z., Ma, P.-L., Ghan, S. J., & Wang, M.: An Evaluation of Marine Boundary Layer Cloud Property  
722 Simulations in the Community Atmosphere Model Using Satellite Observations: Conventional Subgrid  
723 Parameterization versus CLUBB. *Journal of Climate*, 31(6), 2299–2320,  
724 <https://doi.org/https://doi.org/10.1175/JCLI-D-17-0277.1>, 2018a.

725 Song, H., Zhang, Z., Ma, P.-L., Ghan, S., & Wang, M.: The importance of considering sub-grid cloud variability  
726 when using satellite observations to evaluate the cloud and precipitation simulations in climate models.  
727 *Geoscientific Model Development*, 11(8), 3147–3158. <https://doi.org/10.5194/gmd-11-3147-2018>, 2018b.

728 Stephens, G. L., L'Ecuyer, T., Forbes, R., Gettelmen, A., Golaz, J.-C., Bodas-Salcedo, A., Suzuki, K., Gabriel, P., &  
729 Haynes, J.: Dreary state of precipitation in global models. *Journal of Geophysical Research: Atmospheres*,  
730 115(D24), <https://doi.org/https://doi.org/10.1029/2010JD014532>, 2010.

731 Stevens, B. and Feingold, G.: Untangling aerosol effects on clouds and precipitation in a buffered system, *Nature*,  
732 461, 607-613, 10.1038/nature08281, 2009.  
733

734 Suzuki, K., Nakajima, T. Y., & Stephens, G. L.: Particle Growth and Drop Collection Efficiency of Warm Clouds as  
735 Inferred from Joint CloudSat and MODIS Observations. *Journal of the Atmospheric Sciences*, 67(9), 3019–  
736 3032, <https://doi.org/10.1175/2010JAS3463.1>, 2010.

737 Suzuki, K., Stephens, G., Bodas-Salcedo, A., Wang, M., Golaz, J.-C., Yokohata, T., & Koshiro, T.: Evaluation of  
738 the Warm Rain Formation Process in Global Models with Satellite Observations. *Journal of the Atmospheric*  
739 *Sciences*, 72(10), 3996–4014, <https://doi.org/https://doi.org/10.1175/JAS-D-14-0265.1>, 2015.

740 Suzuki, K., Stephens, G. L., & Lebsack, M. D.: Aerosol effect on the warm rain formation process: Satellite  
741 observations and modeling. *Journal of Geophysical Research: Atmospheres*, 118(1), 170–184,  
742 <https://doi.org/https://doi.org/10.1002/jgrd.50043>, 2013.

743 Takahashi, H., Bodas-Salcedo, A., and Stephens, G.: Warm Cloud Evolution, Precipitation, and Their Weak Linkage  
744 in HadGEM3: New Process-Level Diagnostics Using A-Train Observations, *Journal of the Atmospheric*  
745 *Sciences*, 78, 2075-2087, <https://doi.org/10.1175/JAS-D-20-0321.1>, 2021.

Formatted: Font: (Default) Times New Roman, 10 pt

Formatted: Font: (Default) Times New Roman, 10 pt

Formatted: Font: 9 pt

Formatted: Font: (Default) Times New Roman, 10 pt

Formatted: Font: (Default) Times New Roman, 10 pt

Formatted: Font: (Default) Times New Roman, 10 pt

Formatted: Font: (Default) Times New Roman, 10 pt

Formatted: Font: (Default) Times New Roman, 10 pt

746 Wang, H., Easter, R. C., Zhang, R., Ma, P. L., Singh, B., Zhang, K., Ganguly, D., Rasch, P. J., Burrows, S. M.,  
747 Ghan, S. J., Lou, S., Qian, Y., Yang, Y., Feng, Y., Flanner, M., Leung, R. L., Liu, X., Shrivastava, M., Sun,  
748 J., ... Yoon, J. H.: Aerosols in the E3SM Version 1: New Developments and Their Impacts on Radiative  
749 Forcing. *Journal of Advances in Modeling Earth Systems*, 12(1), <https://doi.org/10.1029/2019MS001851>,  
750 2020.

751 Wang, J., Fan, J., Houze, R. A., Brodzik, S. R., Zhang, K., Zhang, G. J., & Ma, P. L.: Using radar observations to  
752 evaluate 3-D radar echo structure simulated by the Energy Exascale Earth System Model (E3SM) version 1.  
753 *Geoscientific Model Development*, 14(2), 719–734. <https://doi.org/10.5194/gmd-14-719-2021>, 2021.

754 Wood, R.: Drizzle in Stratiform Boundary Layer Clouds. Part II: Microphysical Aspects. *Journal of the Atmospheric*  
755 *Sciences*, 62(9), 3034–3050. <https://doi.org/10.1175/JAS3530.1>, 2005.

756 Zhang, G. J., & McFarlane, N. A.: Sensitivity of climate simulations to the parameterization of cumulus convection  
757 in the Canadian climate centre general circulation model. *Atmosphere-Ocean*, 33(3), 407–446.  
758 <https://doi.org/10.1080/07055900.1995.9649539>, 1995.

759 Zhang, M., Xie, S., Liu, X., Lin, W., Zhang, K., Ma, H.-Y., Zheng, X., & Zhang, Y.: Toward Understanding the  
760 Simulated Phase Partitioning of Arctic Single-Layer Mixed-Phase Clouds in E3SM. *Earth and Space Science*,  
761 7(7), e2020EA001125. <https://doi.org/10.1029/2020EA001125>, 2020.

762 Zhang, M., Xie, S., Liu, X., Lin, W., Zheng, X., Golaz, J.-C., & Zhang, Y.: Cloud Phase Simulation at High Latitudes  
763 in EAMv2: Evaluation Using CALIPSO Observations and Comparison With EAMv1. *Journal of Geophysical*  
764 *Research: Atmospheres*, 127(22), e2022JD037100. <https://doi.org/10.1029/2022JD037100>,  
765 2022.

766 Zhang, Y., Klein, S. A., Boyle, J., & Mace, G. G.: Evaluation of tropical cloud and precipitation statistics of  
767 Community Atmosphere Model version 3 using CloudSat and CALIPSO data. *Journal of Geophysical*  
768 *Research: Atmospheres*, 115(D12). <https://doi.org/10.1029/2009JD012006>, 2010.

769 Zhang, Y., Xie, S., Lin, W., Klein, S. A., Zelinka, M., Ma, P.-L., Rasch, P. J., Qian, Y., Tang, Q., & Ma, H.-Y.:  
770 Evaluation of Clouds in Version 1 of the E3SM Atmosphere Model With Satellite Simulators. *Journal of*  
771 *Advances in Modeling Earth Systems*, 11(5), 1253–1268,  
772 <https://doi.org/10.1029/2018MS001562>, 2019a.

773 Zhang, Y., Xie, S., Lin, W., Klein, S. A., Zelinka, M., Ma, P.-L., Rasch, P. J., Qian, Y., Tang, Q., & Ma, H.-Y.:  
774 Evaluation of Clouds in Version 1 of the E3SM Atmosphere Model With Satellite Simulators. *Journal of*  
775 *Advances in Modeling Earth Systems*, 11(5), 1253–1268.  
776 <https://doi.org/10.1029/2018MS001562>, 2019b.

Formatted: Indent: Left: 0", Hanging: 0.5"

777  
778  
779  
780  
781  
782